



Impact of Plasma and Thermal Treatment on the Long-term Performance of Vanadium Redox Flow Electrodes – Significance of Surface Structure vs Oxygen Functionalities

Tobias Greese,^{1,*}  Paulette A. Loichet Torres,^{2,*}  Davide Menga,^{2,*} Petra Dotzauer,¹ Matthias Wiener,³ and Gudrun Reichenauer³

¹ZAE Bayern, Electrochemical Energy Storage, 85748 Garching, Germany

²Chair of Technical Electrochemistry, Department of Chemistry and Catalysis Research Center, Technical University of Munich, 85748 Garching, Germany

³ZAE Bayern, Nanomaterials, 97074 Würzburg, Germany

Graphite felt (GF) electrodes of vanadium redox flow batteries show enhanced performance when thermally treated before their assembly. Thermal treatment works by simultaneously increasing electrode wettability, kinetic activity, and total surface area (TSA). This study examines these performance determining yet inseparable effects, especially considering the electrodes' long-term operation. We exposed GF electrodes to 5 min plasma treatment, ensuring equal wettability, and thermally treated them in air at 400 °C for different durations. We then linked the resulting GF surface structure with the electrode performance, monitored with a high temporal resolution, and controlled electrolyte conditions. The performance, expressed in charge-transfer resistances and voltage efficiencies, correlated accurately with the thermal treatment times. According to XPS, against expectation, the thermal treatment decreased the number of surface oxygen functionalities. Instead, SEM and krypton adsorption revealed that the surface had become rougher, and the TSA increased. Upon corrosion, the surface presumably exposed more carbon edge sites being catalytically active, explaining the improved performance. Therefore, compared with the commonly suggested surface oxygen enrichment, increasing the GF surface roughness and TSA may be the more promising strategy to enhance and stabilize the long-term VRF electrode performance.

© 2021 The Author(s). Published on behalf of The Electrochemical Society by IOP Publishing Limited. This is an open access article distributed under the terms of the Creative Commons Attribution 4.0 License (CC BY, <http://creativecommons.org/licenses/by/4.0/>), which permits unrestricted reuse of the work in any medium, provided the original work is properly cited. [DOI: 10.1149/1945-7111/ac163e]



Manuscript submitted April 7, 2021; revised manuscript received June 24, 2021. Published July 28, 2021.

Supplementary material for this article is available [online](#)

Vanadium redox flow (VRF) batteries store electrical energy environmentally friendly since they employ sustainable materials and promise a long lifetime. For finding widespread use, the batteries must prevail in a competitive market having minimum investment costs. However, realized are minimum investment costs only with an optimized battery cell performance. The cell performance strongly depends on the carbon electrodes, which commonly consist of graphite felt (GF) material. Hence, modifying this GF material bears immense improvement potential for the cell and battery performance.^{1–3} Many different modification techniques have evolved, typically oxidizing the electrode material relying on chemical,^{4,5} electrochemical,^{6–9} plasma,^{10–12} or thermal treatment.^{13–16} Upon oxidation, the electrodes present a substantially enhanced charge-transfer kinetics for the V^{2+}/V^{3+} -reaction, which is the dominating cause for the charge-transfer cell resistance, as opposed to the VO^{2+}/VO_2^{+} -reaction.^{17–19}

The thermal treatment proved to be the most feasible technique with the least processing expenditure, having multiple benefits for the electrode performance. The high temperatures paired with the atmospheric oxygen lead to partial oxidation of the graphite fibers, introducing oxygen-containing surface functional groups. Li et al. attributed the improved V^{2+}/V^{3+} -kinetics to oxygen-containing C–OH groups increasing upon thermal treatment in air at 400 °C for 30 h.²⁰ Similarly, Dixon et al. compared thermally–with plasma-treated graphite electrodes. Low-pressure oxygen plasma treatment (4 min at 60 W generator power) resulted in a higher V^{2+}/V^{3+} -activity than the thermal treatment at 400 °C, reached by a 5 °C min^{−1} heating rate. Their N_2 -BET analysis revealed no increased surface area, so they concluded that the enhanced activity must have resulted from the increased C–OH surface functional groups.¹⁰

Moreover, thermal treatment increases the electrode wettability. Thereby, oxygen functionalities render the fiber surface polar, so the electrode can better saturate with the aqueous electrolyte. Releasing

air pockets otherwise enclosed,²¹ the electrode-to-electrolyte contact area increases, leading to a larger electrochemically active surface area (ECSA).^{22,23} Furthermore, the atmospheric oxygen the treatment involves partially leads to carbon combustion corroding the surface. While the enhanced surface roughness further increases the ECSA, Chu et al. observed that graphite fiber corrosion induced by air oxidation increases the EC surface activity disproportionately with ECSA. Accordingly, this is due to the introduction of carbon edge plane sites. As opposed to carbon basal plane sites, edge plane sites comprise a much higher catalytic activity for EC reactions. Consequently, the surface provides more EC-active sites, implicating both a larger and more active ECSA.²⁴

The trends toward oxygen groups, wettability, surface roughness, and carbon edge sites coincide. Consequently, it has not been possible to identify the thermal treatment's primary benefit for the performance. Providing that the electrodes comprised complete wettability, we pursued this issue, asking 'How is the surface of the carbon fibers affecting the electrode performance, especially in the long-term operation?'

Long-term performance is of particular interest since the GF electrode activity continuously degrades, leading to increased cell overpotentials. In specific, responsible for the increased overpotentials is the electrode sustaining the V^{2+}/V^{3+} -reaction, showing deteriorating reaction kinetics leading to increasing charge-transfer resistance (R_{ct}).^{25–29} In a recent study, we proposed a degradation mechanism being in line with the observed electrode behavior and explaining how the kinetics could decrease over a given time of operation. In short, V^{2+} is assumed to adsorb onto the anode surface during operation with a V^{2+}/V^{3+} -electrolyte, leading to the suggested kinetics deterioration and observed performance degradation.³⁰ In previous research of different groups, identified drivers for degradation are the charging terminal voltage,²⁵ electrolyte temperature,²⁷ electrolyte state-of-charge, and (geometric) electrode current density.²⁸ However, only a few selective studies assayed treatment techniques,^{25,29,31} concluding that electrodes degrade less when thermally treated than in their original form.

*Electrochemical Society Student Member.

²E-mail: Tobias.greese@zae-bayern.de

Accordingly, for systematically modified electrode surfaces, the long-term performance has not yet been under examination.

Consequently, this study investigates how thermal treatment influences electrode activity degradation. The evaluated GF electrodes were pre-treated with plasma before the thermal treatments. This pre-treatment ensured complete electrode wettability, minimizing air inclusions compromising the electrode ECSA. Consequently, in focus is how thermal treatment alters the surface structure, enhancing and stabilizing the electrode performance. Accounting for the continuous performance degradation, we studied the performance not at a given point in time but repetitively over cell operation. For a high temporal resolution of the performance evolution, we required electrochemical techniques that are suitably fast and reliable. Therefore, we repeatedly performed short galvanostatic cell polarization (*short-GCP*). At constant charging and discharging currents at 50% state-of-charge (*SoC*), we measured the cell voltages and derived the corresponding temporary voltage efficiencies. Also, for resolving the altering R_{ct} over time, we employed repetitive potentiostatic electrochemical impedance spectroscopy (*PEIS*). Complementary, we examined the fiber surface structure qualitatively using scanning electron microscopy (*SEM*). Additionally, we used X-ray photoemission spectroscopy to determine the concentration of oxygen groups on the carbon surface, commonly expected to be primarily responsible for catalyzing the vanadium reactions. Moreover, we probed the fiber *TSA* quantitatively using krypton adsorption.

We demonstrate that plasma treatment resulting in a complete electrode wettability and high surface oxygen concentration will not deploy a cell performance for a technical application. Moreover, due to the preceding plasma treatment, the additional thermal treatment did not introduce but instead decrease the oxygen-containing functional groups. After all, the missing correlation of surface activity and oxygen groups questions the general concept that oxygen functionalities are primarily responsible for catalyzing the V^{2+}/V^{3+} -reaction. Instead, the commonly observed increase in functionalities during thermal treatment may only coincide with the concomitant activity increase. In this study, despite decreased oxygen functional groups, the yet enhanced surface activity instead correlated with increased surface roughness and *TSA*, indicating an increase in EC-active carbon edge sites. The resulting *TSA* was decisive not only for enhancing the electrode performance but also for stabilizing it in the long-term cell operation.

Experimental

Electrode modification.—We established equal electrode wettability to investigate how the electrode performance responded exclusively to surface structure alteration. Figure 1 outlines how the electrodes were modified. The electrode material GFD4.6 (SGL Carbon, Germany) is a graphite felt resulting from graphitizing a poly-acrylonitrile (PAN) precursor and consists of 99% graphitic carbon. Figure 1a illustrates the felt material in different magnifications. It reveals its porous structure defined by graphite fibers with a diameter from 8–10 μm . Natively, the graphite fiber surface is non-polar and hydrophobic.

Consequently, when the aqueous, polar electrolyte flows through the electrode, gas inclusions may be trapped²¹ and cause the ECSA to differ randomly from electrode to electrode.²³ Mazur et al. reported graphitic electrodes inhomogeneously wettable even after being thermally treated in air at 400 °C for 9 h.²⁴ As a result, with insufficiently wettable electrodes, it was impossible to reliably correlate the surface structure with the resulting cell performance. Therefore, we pre-treated all GFD4.6 electrodes for 5 min in a PlasmaFlecto 10 low-pressure plasma chamber (Plasma Technologies GmbH, Germany). The chamber was operated with an air atmosphere at 0.3 mbar pressure and 300 W generator power. After the plasma treatment, the electrodes absorbed the electrolyte completely, proving their comprehensive wettability. In the next step, we transferred the electrodes to a preheated KDF-75 box-type furnace (DENKEN-HIGHDENTAL Co., Ltd., Japan) and thermally treated them in air at 400 °C for defined durations of 0, 3, 6, 12, 18, and 24 h. Figure 1b gives an overview of all electrode

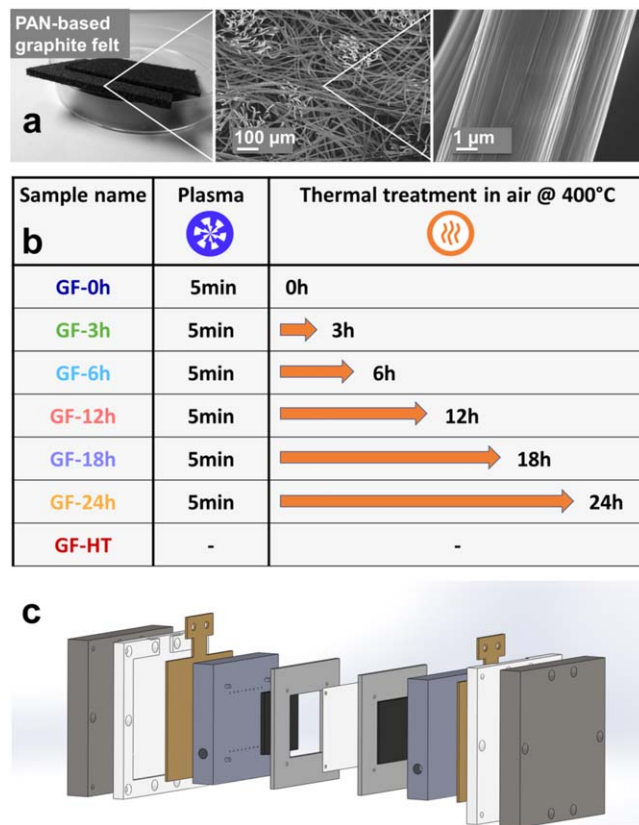


Figure 1. (a) Unmodified PAN-based graphite felt electrode appearing at different length scales. (b) A chart summarizing the performed electrode modifications and the respective sample denotation. For instance, the label GF-24h refers to the graphite felt GFD4.6 that was plasma-treated for 5 min and thermally treated in air at 400 °C for 24 h. (c) Single-cell assembly used for electrode performance tests.

samples and their modification procedure. In addition to the in-house modified samples (GF-0h to –24h), we examined the electrode material GF-HT (SGL Carbon, Germany) as a reference. GF-HT is a commercially available variant of GFD4.6 thermally treated by the supplier (not further specified) and used as received throughout this study.

Single-cell assembly.—For probing the electrochemical performance of the modified electrodes, we employed a VRF single-cell depicted in Fig. 1c. The cell applied the flow-through design with a geometric electrode area of 25 cm². The membrane material was Nafion™ NF212, and monopolar plates were made from an injection-molded graphite-polypropylene composite being chemically inert. The current collectors were gold-coated copper plates. A detailed description of all cell components is available in the supporting information (SI) in Fig. SI 1 (available online at stacks.iop.org/JES/168/070554/mmedia).

Test environment.—As we intended to study how the cell performance changed with the electrode properties rather than the electrolyte, we designed the test environment to keep the electrolyte parameters as stable as possible. Thus, we avoided any possible degradation caused by the electrolyte, eventually affecting the cell performance otherwise. Essential parameters were the electrolyte *SoC*, flow rate, and temperature. We monitored the *SoC* using the open-circuit voltage (*OCV*) by an *OCV* cell (BELLTEC, Germany). Moreover, we automatically adjusted the electrolyte flow rate and the electrolyte temperature. Unless stated otherwise, we recorded all measurements at an electrolyte temperature of $T = 20 \pm 0.2$ °C and a flow rate of $FR = 100 \pm 2$ ml min⁻¹. A schematic of the hardware

and a detailed functional description is also available in the SI in Fig. SI 2. The setup involved VZS005-PP in-line oval-wheel flowmeters (B.I.O.-TECH, Germany), in-line fluor-ethylene-propylene (FEP)-coated Pt100 thermometers (Fig. SI 3a), and an in-house designed plate heat exchanger (Fig. SI 3b). In addition, several NF60 membrane pumps (KNF Neuberger, Germany) were PID-controlled by a customized LabView logic.

Electrolyte preparation and measurement procedure.—The vanadium (V) electrolyte (GfE GmbH, Germany) was at a concentration of 1.6 M V dissolved in 2.0 M aqueous sulfuric acid (H_2SO_4) and ready for use in its uncharged form, referred to as $V^{+III/+IV}$. We pre-charged 500 ml of $V^{+III/+IV}$ to an SoC of 50%, corresponding to an OCV of 1.413 V³² using a conditioning cell (with an arrangement identical to the test cell). After replacing the conditioning cell with the test cell, the measurement program started immediately after the electrolyte filled the electrodes within 30 s.

The program was a sequence of short galvanostatic cell polarization (*Short-GCP*) and potentiostatic-electrochemical impedance spectroscopy (*PEIS*), represented in Fig. 2a as blue and red bars, respectively. The green periods in between mark the time defined as idle cell operation. During this time, the cell voltage was sustained at 1.42 V, so the cell counteracted the slow electrolyte self-discharge across the membrane.

In the *short-GCP*, we probed the cell voltage during a sequence of interchanging charging and discharging current densities $i = \pm 2.5, 20, 40, 60,$ and 80 mA cm^{-2} , as shown in Fig. 2b. The cell voltage U reached constant values for each current density after a

settling time of 30–90 s. Meanwhile, the simultaneously recorded OCV did not change traceably, so the cell entered a quasi-stationary state. We used the respective last constant voltage value to calculate the round-trip voltage efficiency η_V of a short charge-discharge cycle (cf. Fig. 2c). The voltage efficiency, defined as the ratio of energy efficiency (η_E) over coulomb efficiency (η_C), corresponds to

$$\eta_V = \frac{\eta_E}{\eta_C} = \frac{\frac{\int U_{dis}(t)i(t)dt_{dis}}{\int U_{ch}(t)i(t)dt_{ch}}}{\frac{\int dQ_{dis}}{\int dQ_{ch}}} \quad [1]$$

At a constant cell voltage and with $\int i(t)dt = \int dQ$, the voltage efficiency is the ratio of discharging (U_{dis}) over the charging voltage (U_{ch}).

$$\eta_V = \frac{\frac{U_{dis} \int dQ_{dis}}{U_{ch} \int dQ_{ch}}}{\frac{\int dQ_{dis}}{\int dQ_{ch}}} = \frac{U_{dis}}{U_{ch}} \quad [2]$$

For reference, in Fig. SI 4, we plotted the E - i -curves from all of the cell voltages (U_{dis} and U_{ch}) measured throughout 20 h vs their current density.^{1,33}

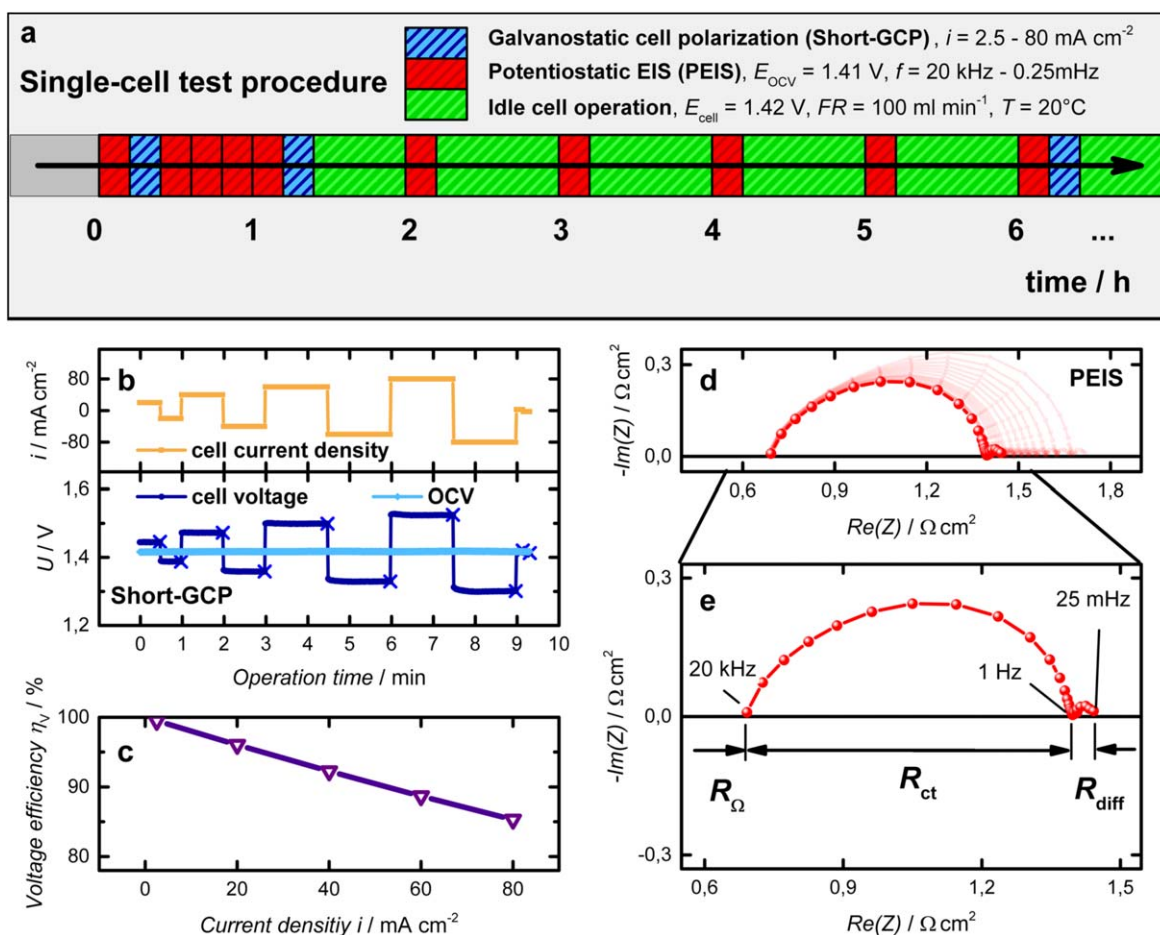


Figure 2. (a) Schematic visualization of the subsequent steps of the measurement procedure applied. (b) *Short-GCP* curves at current densities of $i = \pm 2.5, 20, 40, 60, 80 \text{ mA cm}^{-2}$. (c) Voltage efficiency derived from *short-GCP* cell voltages recorded for different current densities, according to Eq. 2. (d) Nyquist plots of an exemplary sequence of repetitive *PEIS* recorded throughout 20 h of idle cell operation. (e) For better inspection, the Nyquist plot of the first recorded *PEIS*. The voltage oscillated at an amplitude of 30 mV around OCV at frequencies ranging from 20 kHz - 25 mHz. The semi-circle intercepts with the $\text{Re}(Z)$ axis illustrate how the partial resistances R_Ω , R_{ct} , and R_{diff} were derived.

Using *PEIS*, we analyzed the overall cell resistance, distinguishing the kinetic charge transfer from the ohmic and diffusional resistances. During *PEIS*, the voltage oscillated by 30 mV around *OCV* within the frequency ranging from 20 kHz to 25 mHz. One *PEIS* lasted about 10 min. Figure 2d shows the Nyquist plot of all *PEIS* measurements recorded over 20 h. In Fig. 2e, the first of these *PEIS* serves to illustrate the characteristic features used for analysis. The plot features two semi-circles. The first one showed intercepts with the real-part axis at 20 kHz and 1 Hz, while the second one formed between 1 Hz and 25 mHz. We tested in detail how the semi-circles responded to changed system settings, such as the electrolyte temperature ranging between 10 °C–35 °C (Figs. SI 5–7). The first semi-circle appears highly sensitive to temperature changes, while the second semi-circle mainly remained unaltered. Conversely, changing the electrolyte flow rate from 100–25 ml min⁻¹ did not affect the first semi-circle. In contrast, the second semi-circle increased notably (Fig. SI 8). Also, we validated measurement settings such as the *PEIS* voltage oscillation amplitude (Fig. SI 9), ensuring to stay in the linear current-potential region.

On this basis, we identified the intercept of the first semi-circle with the real-part impedance axis at 20 kHz in Fig. 2e to indicate the partial resistance for ohmic conductance (R_{Ω}). At lower frequencies, the first semi-circle diameter between 20 kHz and 1 Hz shows the reaction kinetics resistance R_{ct} . Finally, at the lowest frequencies between 1 Hz and 25 mHz, the diffusional mass transport resistance R_{diff} appears.³⁴ Therefore, in the context of this research, we determined R_{Ω} , R_{ct} , and R_{diff} by linearly extrapolating the semi-circles to the real-part impedance axis. Indeed, the measured resistance data included additional factors. For instance, the inductance of the circuit influenced the resistance at high frequencies > 10 kHz. Moreover, the electronic and ionic conductance contributed to the resistance at medium frequencies 20 kHz > f > 1 Hz, according to the transmission line model.³⁵ However, since these factors were invariant over time, we consider them not to interfere with the present research results.

Scanning electron microscopy (SEM) and krypton adsorption analysis.—We investigated the electrode surface for its microscopic appearance using a Zeiss Ultra 55 plus instrument. We analyzed the samples (without special preparation) using the Inlens-detector at an acceleration voltage of 10 to 12 keV.

Additionally, we examined the specific surface area with krypton adsorption at 77.4 K performed with an Autosorb iQ2 (Quantachrome Instruments, USA). The area was calculated using the Brunauer–Emmett–Teller (*BET*) method. Before analysis, we degassed the samples at 300 °C for at least 24 h. Due to the relatively small surface area, in order to obtain reliable results, about 1 g of sample was used for each analysis.

X-ray photoelectron spectroscopy.—X-ray photoelectron spectroscopy (*XPS*) was employed to monitor the changes in the oxygen groups present at the surface of the evaluated GF electrodes, focusing on the C 1s and O 1s regions. The GF electrodes were cut into 25 mm² samples and mounted conducting on a stainless steel sample holder. All *XPS* spectra were recorded at 40 eV pass energy, a 0.1 eV step size, and a 1000 ms dwell time with an Axis Supra system (Kratos, UK) using a monochromatic Al K α source (1486.6 eV). For each sample, an initial survey scan was recorded, followed by a high-resolution spectrum of the elements of interest. Each spectra's binding energies were corrected based on the adventitious carbon signal from the C 1s spectrum at 284.4 eV. The O/C ratio was calculated from the relevant peak areas, integrated using a Shirley background for the O 1s region and a 2 U Tougaard background for the C 1s region using the CasaXPS software (Version 2.3.22PR1.0). All areas were normalized by the corresponding atomic subshell photoionization cross-section³⁶ and the escape depth, predicted using the NIST Electron Effective-Attenuation-Length Database.³⁷

Results and Discussion

Nyquist plots and voltage efficiencies throughout the first 20 h of idle operation.—Figure 3a shows the Nyquist plots of the repetitive *PEIS* of a VRF single-cell with the differently modified GF electrodes (see Fig. 1b for the electrode modification). From top to bottom, the duration of thermal treatment in air at 400 °C is increasing. The bottom plot represents the commercial reference electrode GF-HT thermally treated by the supplier. Each graph represents one electrode modification monitored over their first 20 h after initial contact with the 50%-charged vanadium electrolyte. All Nyquist plots comprise two characteristic semi-circles, the first pronounced ones representing R_{ct} and the second smaller ones R_{diff} . With all GF electrodes, we observed that the first R_{ct} semi-circle increased with the idle operation time. We plotted the R_{ct} values for each GF electrode as a function of the idle operation time in Fig. 3b. R_{ct} increased continuously, regardless of the electrode modification applied previously. However, in absolute terms, both the initial R_{ct} and the rate of increase $\Delta R_{ct}/\Delta t$ became smaller for longer thermal treatment times.

The GF-0h serves here as a control sample since it has only been treated with plasma to increase the electrode wettability, as seen in Fig. 1b. In Fig. 3c, we normalized each R_{ct} to the respective R_{ct} of sample GF-0h to disregard any contribution from the plasma treatment. The resulting ratios indicate that thermal treatment further enhanced the absolute electrode activity distinctly. After just three hours of heat treatment, R_{ct} decreased by 50% (green in Fig. 3c) and by 78% after 24 h of heat treatment. GF-HT as a commercially available GF variant showed the lowest R_{ct} of the evaluated samples being only 15% of the value of GF-0h.

Additionally, we normalized each series of R_{ct} to its respective first measured value at the beginning of each repetitive *PEIS* sequence in Fig. 3d. Indeed, the tested samples differed significantly by their absolute R_{ct} . However, in relative measures, their R_{ct} increased similarly, by a factor of 1.5 ± 0.2 over the first 20 h of operation. Moreover, GF-HT showed a similar degradation with a 1.5-time increase, as did the in-house plasma- and thermally treated samples. Thus, the similar degradation of GF-HT lacking the plasma treatment indicates no correlation between performance degradation and plasma treatment. Instead, it suggests that degradation as a general phenomenon is independent of electrode modification.

Using the *short-GCP* technique complementary to *PEIS*, we analyzed the voltage efficiency η_V . In Fig. 4a, we show the η_V for GF-0h, GF-3h, and GF-24h at current densities ranging from 0–80 mA cm⁻². Additionally, in Fig. 4b, we plotted them over the elapsed time of idle operation from 0–20 h. The trends observed in Fig. 4 reflect the features already noticed in the *PEIS* measurements. As these features became most evident for high current densities, we will focus on the analysis of the η_V at 80 mA cm⁻². As expected from the R_{ct} trends, the η_V of GF-0h started at a lower value of 85.3%, whereas GF-24h began at 91.0%, which accounts for a 5.7% higher efficiency. Regarding the idle operation time, agreeing with the R_{ct} trends, we observed that the η_V decreased with time on the three electrodes evaluated. However, between the electrodes with different treatment times, the extent of η_V decrease varied, being less pronounced on the electrodes subject to longer treatments. Accordingly, η_V of GF-0h shows a marked drop of 2.1% (i.e., from initially 85.3% at 0 h to 83.2% at 20 h). In contrast, the η_V of GF-24h decreased by only 0.3% (i.e., from initially 91.0% at 0 h to 90.7% at 20 h). The η_V of the GF-3h electrode estimated at 80 mA cm⁻² falls between the η_V of GF-0h and GF-24h, reflecting the trends in R_{ct} . In general terms, the longer the thermal oxidation lasted, the smaller the decrease in η_V was over idle operation time.

Given all of the analogies between *PEIS* and *short-GCP* identified, one might conclude that both techniques assess the cell performance and reveal quantitative data likewise. However, the perspective of these two sets of performance data is different. On the one hand, *short-GCP* showed how internal processes in the cell intervene in the performance overall and translate into a practical

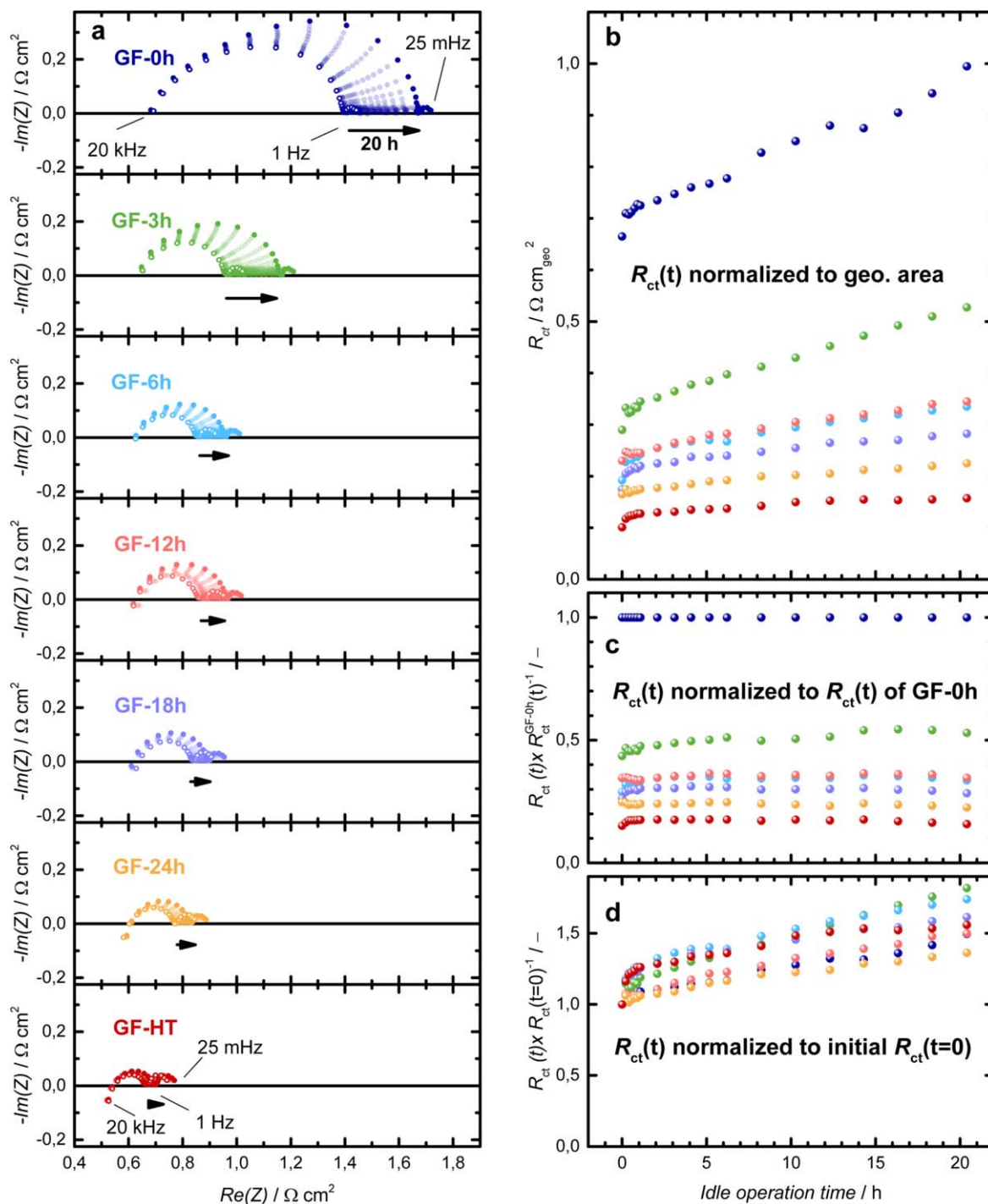


Figure 3. (a) Nyquist plots of repetitive PEIS over 20 h of initial idle operation for all modifications of the graphite felt electrodes investigated. From top to bottom: Electrodes were thermally treated in-house for increasing durations at 400°C (GF-0h - GF-24h) and thermally treated by the supplier (GF-HT). (b) charge-transfer resistances R_{ct} over 20 h of idle cell operation, normalized to the geometric electrode area of 25 cm^2 . (c) R_{ct} over idle operation time, each point in time normalized to the respective value for the GF-0h sample, relating the different electrodes to each other. (d) R_{ct} over idle operation time, normalized to its initial value at $t = 0$, showing each relative R_{ct} increase ratio.

meaning for technical applications. For instance, the only plasma-treated electrodes showed low efficiency from the beginning, which continued to degrade fast. Thus, particularly when considering a long-term operation, we conclude that their economic viability for technical purposes is questionable. On the other hand, PEIS provided a greater depth of information when distinguishing between partial resistances. In the present study, this distinction revealed that the change in performance was due to a changing R_{ct} , which, in turn, implies changes on the electrode surface.

We learned that the electrode performance improved dramatically upon thermal treatment. However, since the plasma pre-treatment resolved the wettability problem, why did the thermal treatment enhance the performance, corresponding so strictly with the treatment duration? Is the performance improvement dominated by a change in surface structure or an increase in surface oxide groups? Addressing these questions, in the next section, we will investigate how the surface structure and its TSA changed as a result of thermal treatment for different treatment times.

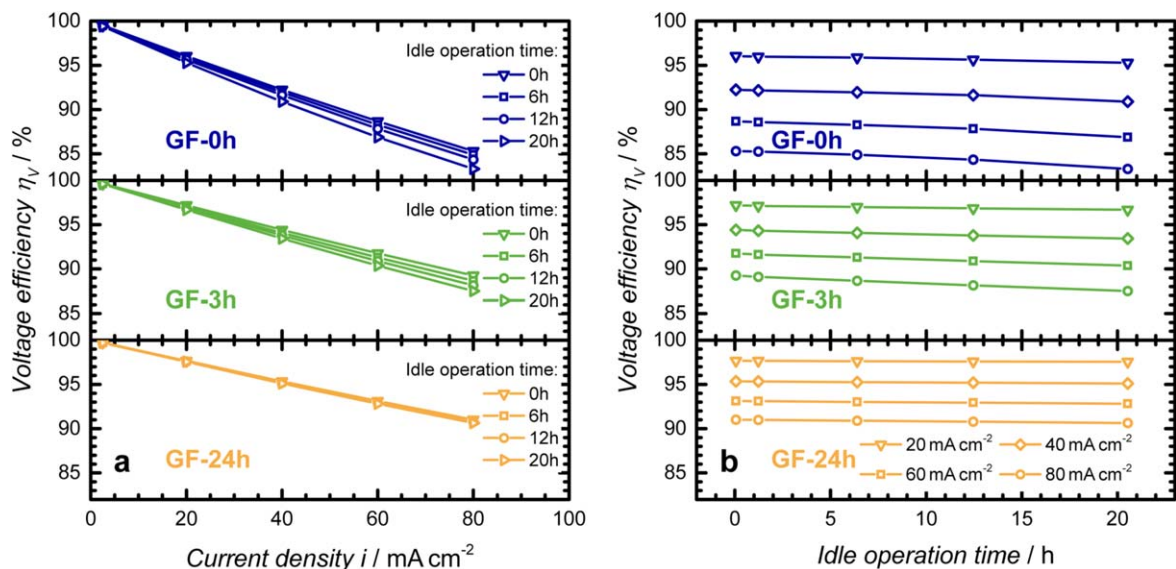


Figure 4. Voltage efficiencies from repetitive *short-GCP* single-cell measurements of GFD4.6 graphite felt electrodes after plasma and subsequent heat treatment at 400 °C for the duration of 0 h (blue), 3 h (yellow), and 24 h (green) in idle cell operation at an SoC of 50%. (a) Voltage efficiency vs current density at different points in time (after 0, 6, 12, and 20 h of idle operation). (b) Voltage efficiencies vs idle operation time over 20 h.

Scanning electron microscopy (SEM).—We examined the surface structure of single fibers of the different electrode modifications using SEM micrographs. Figure 5 compares the images of four treated electrodes. The three upper rows show GF-0h, GF-12h, and GF-24h, which we modified in-house; the lower row depicts GF-HT modified commercially. The left images represent a 4,000-fold magnification (Figs. 5a, 5c, 5e, and 5g). For better inspection, the images on the right zoom with 40,000-fold magnification (Figs. 5b, 5d, 5f, and 5h).

In this context, GF-0h served as a reference material that was only plasma-treated but did not experience any corrosive thermal treatment (Figs. 5a and 5b). Consequently, disregarding the native rills and grooves with smooth edges, no defects can be found on its surface. Surprisingly, GF-12h thermally treated in air at 400 °C for 12 h showed no visible change (Figs. 5c and 5d). Eventually, the situation appeared different for GF-24h (Figs. 5e and 5f). The previously smooth edges seem nibbled, thus receiving a fringed structure visible with the 40,000-fold magnification. Finally, the trend culminates for GF-HT. While already recognizable in Fig. 5g on the left, it is eye-catching at 40,000-fold magnification in Fig. 5h. The surface resembled a cratered landscape, and the former grooves were only vaguely retraceable. Instead, an array of adjacent surface pores appeared, with pore sizes in the order of 50 nm. Given this evident increase in surface roughness, we also expected the specific surface area to increase.

Krypton adsorption and BET analysis assessing the total surface area (TSA).—To quantify these SEM observations, we assessed the electrode surface areas by krypton adsorption and calculated the corresponding BET surface area (S_{BET}), interpreted as the TSA and summarized in Fig. 6a. The thermal treatment increased the TSA with time. While the TSA of the as-received felts (GF-ar) increased only marginally by 4% from 0.49 to 0.51 $\text{m}^2 \text{g}^{-1}$ ($\pm 0.03 \text{m}^2 \text{g}^{-1}$) after the plasma pre-treatment, the subsequent thermal treatment had a more substantial effect on the TSA. After the first three hours of thermal treatment (GF-3h), the surface area increased by 8% to $0.55 \pm 0.03 \text{m}^2 \text{g}^{-1}$. A longer treatment duration caused a continuous increase in TSA by 0.02 ($\text{m}^2 \text{g}^{-1}$) h^{-1} until, after 24 h, the TSA had doubled. The increased TSA of the GF-24h sample agreed with the SEM images showing a higher surface roughness due to the apparent fringed structure. While the SEM images for the GF-12h sample failed to visualize any structural changes, krypton adsorption resolved a significant surface area increase for treatment durations

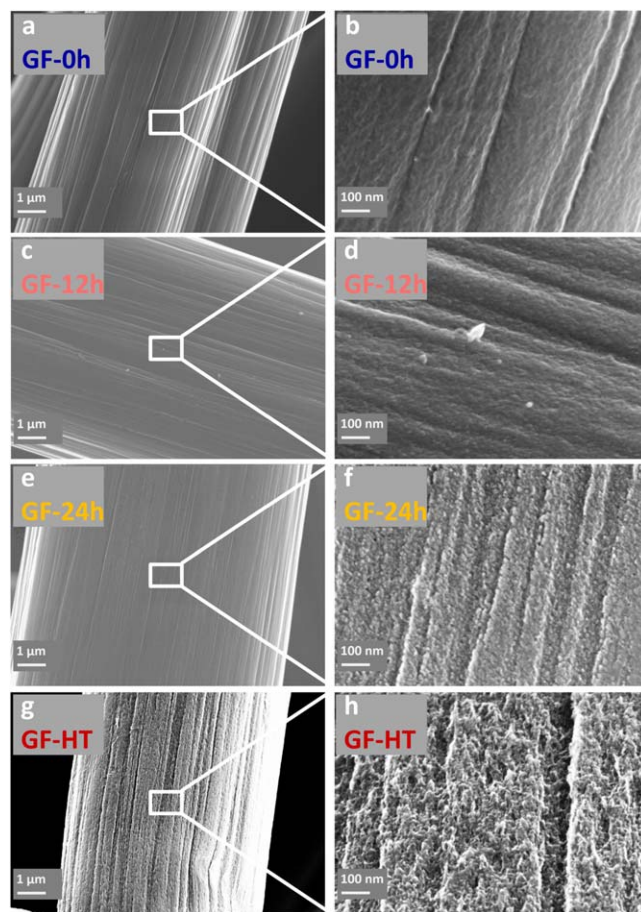


Figure 5. SEM micrographs of GF-0h (a), (b), GF-12h (c), (d), GF-24h (e), (f), and GF-HT electrodes (g), (h), with 4,000-fold magnification shown on the left, and 40,000-fold magnification on the right, respectively.

shorter than 24 h. For the GF-HT sample, the situation is even more distinct. According to the SEM images, this sample displayed the roughest surface (cf, Figs. 5g and 5h). In agreement with this observation, the S_{BET} of the GF-HT sample was $6.11 \pm 0.03 \text{m}^2 \text{g}^{-1}$

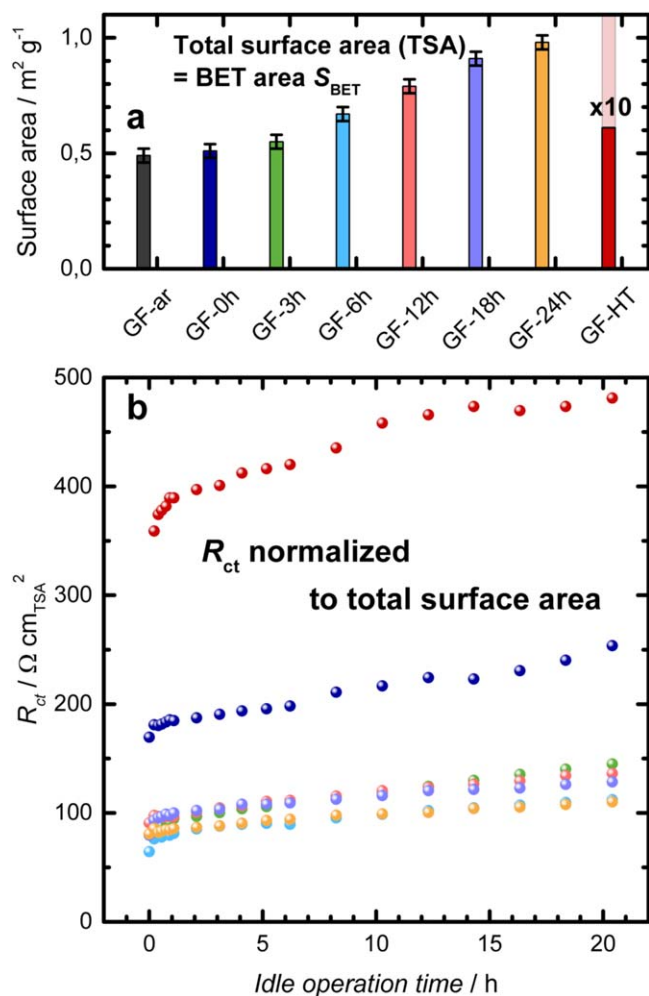


Figure 6. (a) Surface areas calculated from the *BET* analysis of krypton adsorption, interpreted as total surface areas (*TSA*). (b) R_{ct} normalized to the *TSA* derived from krypton-*BET* analysis.

⁻¹. This value corresponds to an increase in *TSA* of 520% compared to the sample GF-24h.

To test how the electrode kinetics relates to the actual carbon surface area, we normalized the R_{ct} from Fig. 3 to the *TSA* (see Fig. 6b). Interestingly, the GF-0h and GF-HT electrodes presented higher R_{ct} normalized to the carbon area than the other electrodes. GF-0h comprised twice the R_{ct} of GF-3h to –24h, whereas GF-HT showed even four times higher values, which will be discussed in the next section. All the other electrodes (GF-3h to –24h) showed comparably equal R_{ct} , being around $100 \Omega cm^2$ during the first 20 h of operation, confirming the EC performance to correlate with surface structure.

Other than structure, the surface composition remained to be examined. Not least accounting for the deviating GF-0h and GF-HT, the observed kinetics may have resulted from the accumulation of surface functionalities. The most prominent are surface oxides commonly attributed to a high catalytic activity, which we will examine below.

X-ray photoelectron spectroscopy (XPS) assessing the oxygen surface content.—We used XPS to examine how the carbon surface's atomic composition changed following the electrode modifications. Figures 7a–7c present exemplary spectra taken from the C 1s and O 1s regions. Figure 7a shows the O 1s region normalized by the maximum intensity of the respective C 1s peak (284.4 eV) for each sample. This comparison is done only for a selected set of treated GFs, to illustrate the differences in oxygen

content on each of the GF samples. Figures 7b and 6c show another type of normalization for both the C 1s and O 1s regions. The C 1s and O1s peak intensities were normalized by the C 1s and O 1s regions' maximum intensity. The aim was to get a qualitative comparison of the overall peak shape and evaluate the possibility of different oxygen species present on each modified electrode. In Fig. 7a–7c, we selected the GF-ar, GF-0h, and GF-HT as reference electrodes to be compared with GF-24h, the electrode with the most prolonged thermal treatment done for 24 h. At first glance, the spectra suggested evident differences in the oxygen content between reference and thermally treated electrodes. We quantified this difference by the ratio of the individual C 1s and O 1s peak areas, known as the O/C-ratio, measuring the electrode surface's oxygen content (Fig. 7d). A comparison of GF-0h with GF-ar in Fig. 7a clearly shows that the sole plasma treatment extensively enriched the surface with oxygen. This enrichment is also evident in Fig. 7d in the O/C ratio, which increased from 2.4% (GF-ar) to 16.0% (GF-0h). This increase confirmed that the electrodes became more wettable after the plasma treatment because the number of oxygen surface groups increased.

The O/C-ratios for the electrodes thermally treated in air at 400 °C were different than expected. Reports in the literature suggest that a more aggressive (500 °C)¹⁷ or prolonged (30 h)^{20,29} thermal treatment increases the surface oxides. However, Eifert et al. reported that this was not the case for the evaluated treatment (in air at 400 °C for 25 h).³⁸ Our data also showed that further thermal treatment combined with preceding plasma treatment did not increase the oxide concentration but had the opposite effect. After only three hours (GF-3h), the surface oxide groups decreased to less than half of the value for GF-0h, from 16% down to 7%. No clear trend emerged for the electrodes with more prolonged treatment time, and their O/C ratio remained at $8 \pm 2\%$, at about half the level than GF-0h.

The O 1s peaks represent many different surface oxide groups, including hydroxyl, carbonyl, or carboxyl functionalities.³⁹ Thereby, each species may catalyze the presumably inner-sphere V2+/V3 + -reaction to different extents characterized by its site-specific rate constant. Consequently, some distinct oxides may be responsible for the gross activity. There are many opinions in the literature on how the XPS technique can identify specific surface species catalyzing the vanadium reactions. This variety resulted in many different interpretations of the XPS spectra, attributing the increased electrode performance to different species such as C–OH^{4,10,20,40,41} C=O,^{7,40,42} and COOH groups.^{7,11,41} However, this interpretation is susceptible to the type of line shape and background used to fit the XPS spectra. Thus, we opted for just a qualitative comparison of the spectra focussing on the integral O/C ratios rather than on individual oxygen species potentially influencing the electrode performance. Thereby, the O 1s peak shape in Fig. 7b did not qualitatively vary among the presented samples, suggesting that the composition of oxygen surface groups remained the same. Similarly, the C 1s peak comparison between the GF-24h and GF-HT electrode in Fig. 7c showed almost identical peak shapes, a trend persisting for all the thermally treated electrodes GF-3h—GF-24h. As a result, the identical peak shapes did not identify specific surface groups responsible for the performance improvement.

When accounting for the *BET* results, the GF-24h electrode surface comprised two times the *TSA* but only half the O/C ratio, compared to GF-ar, suggesting that its total oxide amount remained constant. Hence, for the evaluated thermally treated GF electrodes, a surface oxide increase cannot explain the simultaneous fivefold increase in EC activity (cf, Fig. 3c). Instead, some other surface property must be associated with the reduced R_{ct} . Judging from the observed R_{ct} correlation with *TSA*, this property is most likely related to the surface structure.

Resolving changes in surface structure with *SEM* was difficult for GF-3h - GF-12h. However, GF-24h eventually revealed a change in surface appearance. Its fringed form proved that the mild treatment at 400 °C corroded the topmost carbon layers. In an idealized picture,

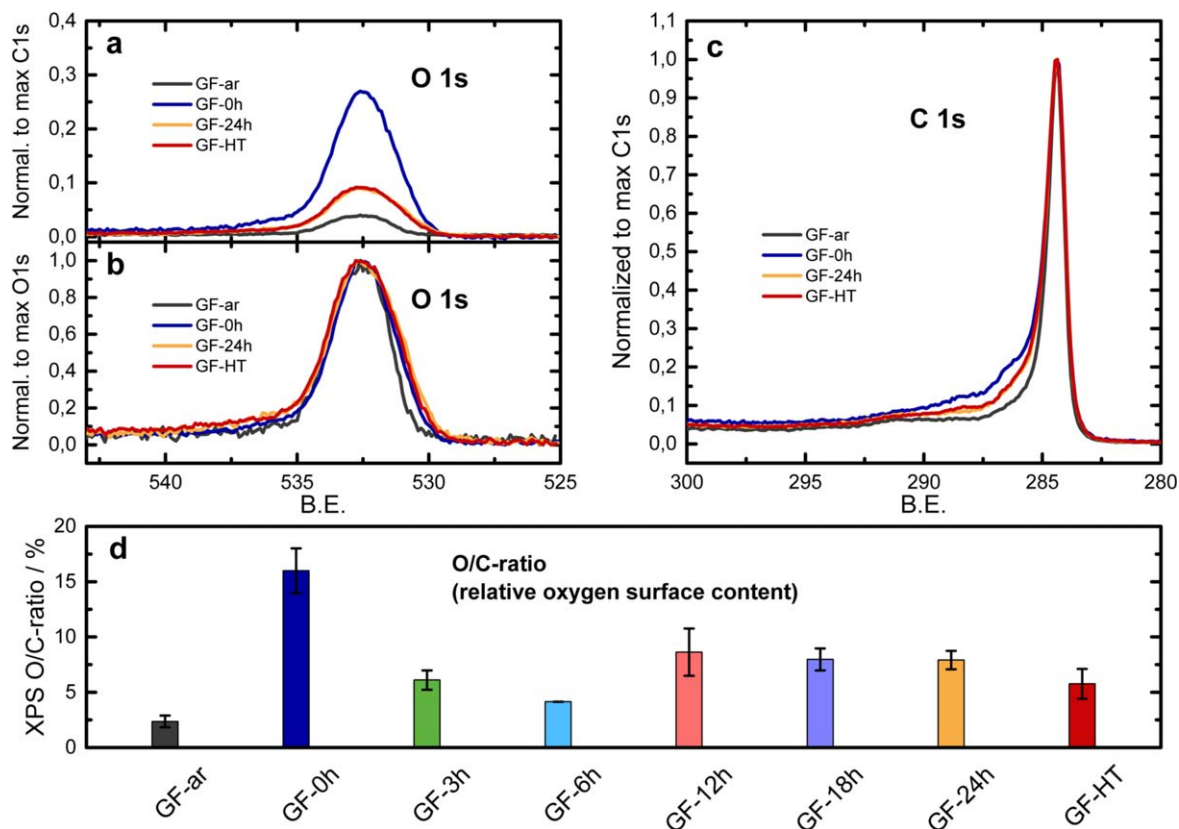


Figure 7. (a) O 1s XPS spectrum normalized by the maximum intensity of the respective C 1s peak (284.4 eV) of the reference samples GF-ar, GF-0h, and GF-HT, and the thermally treated electrode GF-24h. (b) O 1s and (c) C 1s XPS spectra normalized by the maximum intensity of the individual O 1s (532.5 eV) and C 1s (284.4 eV) regions presented for the reference electrode GF-ar, GF-0h, and GF-HT and the thermally treated electrode GF-24h. (d) O/C ratio obtained from peak areas of the individual C 1s and O 1s regions for the reference and thermally treated GF electrodes.

the top layers constitute ordered and electrochemically inactive basal planes.⁴³ When thermal treatment sets in, these basal planes start to corrode. Over time, at defects, edges, and corners, corrosion proceeds to “eat away” carbon after carbon along the basal plane, leaving behind more and more edge sites instead.^{24,44,45} Compared to basal sites, edge sites comprise much higher catalytic activity for inner-sphere reactions,^{46,47} including the V^{2+}/V^{3+} -reaction.^{48,49} This higher activity may explain the disproportionate performance improvement observed with TSA.

However, krypton adsorption does not differentiate between basal and edge sites. Consequently, considering the sites’ diverging specific activity, we cannot expect a linear correlation between R_{ct} and TSA. Instead, R_{ct} may be linearly proportional to the surface area constituting only graphitic edge sites. As proposed by Rabbow and Whitehead, this edge site area is accessible by deconvoluting the electrochemical double-layer capacitance (EDLC).⁵⁰ The EDLC consists of contributions from relatively inactive basal carbon planes and edge planes accounting for the active surface area (ASA). Thereby, the edge planes contribute much more to the EDLC than basal planes (cf, $1\text{--}3 \mu\text{F cm}^{-2}$ from basal planes vs $50\text{--}100 \mu\text{F cm}^{-2}$ from edge planes).^{51–53} Rabbow et al. have demonstrated that the knowledge of the TSA and the EDLC generally suffices to determine the size of the ASA. By describing the basal plane surface as the difference $TSA-ASA$, the EDLC is an expression of the edge and basal plane contributions corresponding to

$$EDLC = (TSA - ASA) \cdot c_{basal} + ASA \cdot c_{edge} \quad [3]$$

The carbon surface-specific capacitances were determined to $c_{basal} = 3.2 \mu\text{F cm}_{carbon}^{-2}$ and $c_{edge} = 47.8 \mu\text{F cm}_{carbon}^{-2}$. Solving Eq. 3 yields the ASA as

$$ASA = \frac{EDLC - TSA \cdot c_{basal}}{c_{edge} - c_{basal}} \quad [4]$$

Consequently, we sought to assay the electrodes’ EDLC by cyclic voltammetry (CV) and PEIS (cf, Fig. SI 10). For doing so, we vacuum-infiltrated the electrodes at low pressure < 3 mbar for 3 min each. The gravimetric capacitance values derived by PEIS at 0.15 V vs Hg/Hg₂SO₄ match the range of the ones measured by Rabbow et al., with GF-0h and GF-HT presenting 33 mF g^{-1} and 298 mF g^{-1} , respectively. Unfortunately, the plasma and thermally treated electrodes showed no unambiguous trend with thermal treatment time, so we assessed the results as not reliable enough for further conclusions. Presumably, the different amounts of surface oxides concentrations causing pseudo-capacitance by faradaic reactions superimposed the double-layer capacitance. This assumption derives from the following observation. When exposed to a second plasma treatment, the thermally treated electrodes exhibited an up to 60% increase in capacitance, illustrating the significant capacitance variation due to additional surface oxides. Accordingly, it deemed not reasonable to derive any robust conclusions from the capacitance data, e.g., to derive the ASA and correlate it with performance.

The relative effect from pseudo-capacitance is presumably low for the two samples GF-0h and GF-HT, differing substantially in TSA. For those electrodes, the ASA, according to Eq. 4, was at $380 \text{ cm}_{edge}^{-2} \text{ g}^{-1}$ and $2300 \text{ cm}_{edge}^{-2} \text{ g}^{-1}$, respectively, being again in good agreement with the data of Rabbow et al. These values of ASA correlate much closer with the R_{ct} than the ones for the TSA. This relation explains why the TSA-specific R_{ct} in Fig. 6b showed much higher values than those of the other modifications. The increased TSA may predominantly comprise basal carbon planes contributing

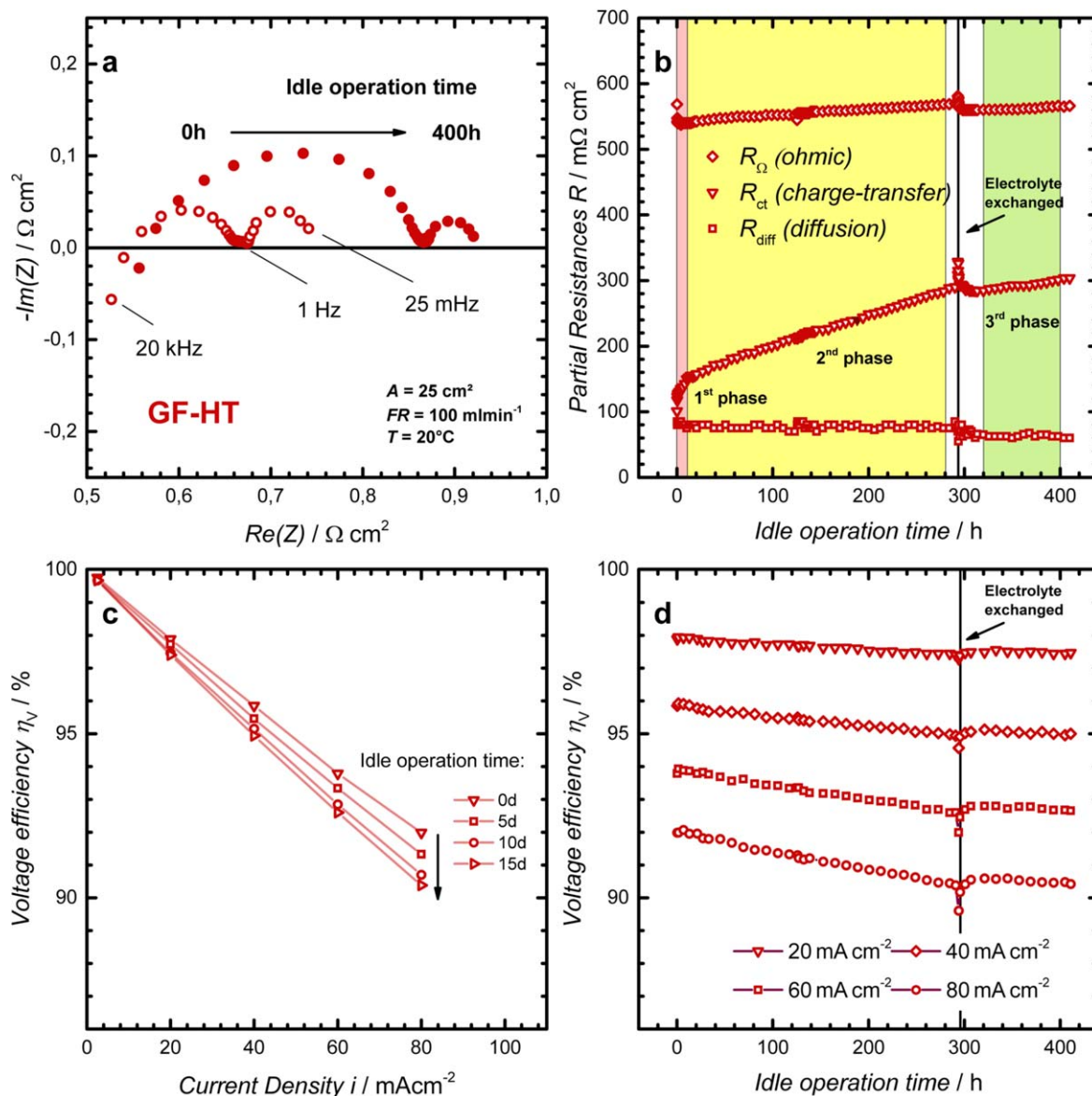


Figure 8. (a) Nyquist plots of repetitive PEIS single-cell measurements for commercially available GF-HT electrodes (SGL Carbon) for a duration of 400 h (16.7 d) in idle cell operation at an SoC of 50%. The open circles represent the first PEIS recorded right after initial electrolyte contact (0 h). In contrast, the filled circles are the PEIS recorded after 400 h of idle operation. (b) Respective separated partial resistances vs idle operation time over 400 h. (c) Voltage efficiency vs. current density at different points in time (after 0, 5, 10, and 15 d of idle operation). (d) Voltage efficiencies vs idle operation time over 400 h.

to the kinetics enhancement less than the edge planes do. This situation demonstrates that the performance differences might be solely explainable by differences in carbon edge planes.

Although the ASA is hard to estimate, the proposed surface transition can explain why the R_{ct} halved after only 3 h of thermal treatment compared to sample GF-0h. The basal plane corrosion may have led to a substantial edge site formation.^{23,24,45} On the atomic scale $< 1 \text{ nm}$, corrosion would have continuously accumulated more and more edge sites, contributing a disproportionately large share to the surface-specific catalytic activity. Therefore, thermal treatment is effectively altering the surface structure, long before becoming visible by SEM and only implicated by krypton adsorption analysis. The resulting increase in edge sites could be responsible for the observed pronounced enhancement in EC surface activity.

Due to the small absolute R_{ct} of sample GF-HT, its performance appeared almost stable throughout the short-term operation of 20 h. Therefore, the GF-HT was selected to evaluate the performance trends for long-term operation. To do so, we measured the GF-HT performance for a more extended operation period of 400 h. Again,

all system settings such as temperature, flow rate, and SoC were constant throughout this period.

Monitoring commercial GF-HT electrodes over 400 h of idle operation.—We investigated the graphite felt GF-HT for its long-term electrode performance. GF-HT is another modification variant of GFD4.6, thermally treated by its supplier SGL Carbon. Possibly adjusted treatment parameters were the temperature and duration.¹³ Also, the treatment atmosphere can have a significant impact, more specifically, the atmosphere's content of water⁵⁴ and oxygen.¹⁴ Although the modification procedure was not specified, the electrode presented a specific TSA of $6 \text{ m}^2 \text{ g}^{-1}$, the highest TSA evaluated. Consequently, as a commercially available material with an optimized surface area and a superior 20 h performance, GF-HT attracted interest to be studied for a more extended period of 400 h.

Throughout 400 h, we continuously pumped the electrolytes at 100 ml min^{-1} flow rate, 50% SoC, and 20°C temperature through the 25 cm^2 GF-HT electrodes mounted in the single-cell. During this time, we intermittently probed the cell with repetitive PEIS and short-GCP. Figure 8a represents Nyquist plots of the first and the

last PEIS, while Fig. 8b illustrates the three partial resistances R_{Ω} , R_{ct} , and R_{diff} separately over the idle operation time. Overall, the familiar trend of increasing R_{ct} appears. By comparison, R_{Ω} and R_{diff} remained constant, but R_{ct} increased steadily, from 120 m Ω cm² to 300 m Ω cm².

Interestingly, the rate of increase $\Delta R_{ct}/\Delta t$ took on distinctly different values associated with three phases. The first phase emerged during hours 0–10 (light red area in Fig. 8b), where R_{ct} rose with a steep slope from 120 m Ω cm² to 150 m Ω cm², and the increase rate amounted to 3.0 m Ω cm² h⁻¹. The second phase followed between hours 10–290 (yellow area in Fig. 8b); R_{ct} grew linearly from 150 m Ω cm² to 290 m Ω cm² but at a much slower rate of 0.5 m Ω cm² h⁻¹ being a sixth of that during the first phase. Finally, in a third phase (green area in Fig. 8b), the inclination became low between hours 320–400, elevating from 285 m Ω cm² to 300 m Ω cm². The rate of increase in this last phase was 0.2 m Ω cm² h⁻¹, which was only a fifteenth of the pace during the first 10 h.

During the first and second phases up to hour 290, the cell operated on the same original electrolyte. Eventually, the tank filling levels differed by 20%, pointing at a directed electrolyte transport. Pezeshki et al. found that the accompanying vanadium crossover leads to a shift in reactant concentrations, causing the electrolyte to be increasingly imbalanced.²⁸ Moreover, oxygen diffusion via the tubing adds to this effect.⁵⁵ This electrolyte imbalance may have contributed to the linear R_{ct} increase in the second phase. Therefore, after 290 h, we exchanged the potentially imbalanced electrolyte. With N₂ overpressure, we flushed the electrolyte out of the tanks, the tubing, and the measuring cell. We then replaced the measuring cell with the conditioning cell, refilled the system with fresh V^{+III}/V^{+IV}, and pre-charged the new electrolyte to 50% SoC. Finally, we returned the measuring cell, re-flooded the electrodes, and continued the performance test. From hour 320 on, the trajectory of R_{ct} followed a flatter course, reflecting the fresh, balanced electrolyte.

However, before, between hours 290–320, a pronounced peak in R_{ct} appeared, with R_{ct} jumping from 290 to 330 m Ω cm² and dropping back to about 285 m Ω cm² during the next 30 h. We attribute the feature to entrapped gas remaining in the electrodes after the electrolyte exchange, temporarily compromising the ECSA. Presumably, during hours 290–320, the continuous electrolyte flow dragged out the gas inclusions, explaining that R_{ct} resumed its previous course of a slow increase. Accordingly, the R_{ct} drops from 330 m Ω cm² to 285 m Ω cm² due to improving electrode saturation accounting for 45 m Ω cm² of additional R_{ct} . In relative measures, this corresponds to $45/285 = 16\%$ of electrode volume that was not contacting the electrolyte after the system refill. This figure is consistent with the observations of Bevilacqua et al., where the electrolyte saturation of graphite felt electrodes showed to increase from 73% to 78% after the first few minutes of electrolyte flow-through.²¹ As a remark, the heat-treated electrodes from the previous section might have faced a similar, slight constriction in ECSA upon initial electrolyte saturation. Indeed, the ECSA and, in specific, the ASA proved hard to estimate. However, the strong correlation of the electrodes' respective R_{ct} with treatment time and TSA suggests that the deviations in electrolyte saturation were very comparable to each other. Interestingly, this effect of progressive ECSA increase with electrolyte saturation counteracts the observed initial R_{ct} increase due to kinetic degradation. The situation where both effects balance each other explains why the initial kinetic degradation may be unnoticeable in some studies found in the literature.

In the third phase, between hours 320 and 400, notably, R_{ct} was now at slightly smaller values, 10 m Ω cm² less, reflecting the new, balanced electrolyte. Moreover, R_{ct} rose distinctly slower than in the first 10 h, at a fifteenth growth rate. The decelerating rate agrees with studies observing the degradation to slow down over eight days of operation (168 h).²⁷ If continuing, this trend may predict that the R_{ct} increase will become insignificant at some point, or R_{ct} even converges to a constant value.

The observed trend of decelerating degradation agrees well with the concept of an adsorbant leading to the degradation, as we proposed in a previous study.³⁰ Accordingly, V²⁺ adsorbs to the reaction surface, covering it and, thus, inhibiting the further V²⁺/V³⁺-reaction. Over time of operation and contact to V²⁺, an equilibrium coverage will form, leaving behind an uncovered ECSA (A_{ECSA}). Then, the temporal evolution of the A_{ECSA} being not yet covered and deactivated by an adsorbent can be expressed as

$$A_{ECSA} = A_{ECSA,0} \left((1 - \theta) + \sum_i \theta \cdot e^{-k_i t} \right) \quad [5]$$

Here, $A_{ECSA,0}$ stands for the initial fully uncovered ECSA before in contact with V²⁺/V³⁺-electrolyte. Moreover, θ is the relative equilibrium coverage, k_i the decay constants, and t the idle operation time. With R_{ct} being inversely proportional to A_{ECSA}

$$R_{ct} \propto (A_{ECSA})^{-1}, \quad [6]$$

the trajectory of R_{ct} can be fitted by Eq. 5 with two decay constants ($i = 2$). This perception of an equilibrium coverage explains why the observed degradation process decelerates and provides another strong argument for a converging R_{ct} .

For practical purposes, *short-GCP* (Fig. 2) allowed translating the corresponding performance into voltage efficiencies (η_V) according to Eq. 2. In Fig. 8c, we plotted η_V vs the current density measured after selected idle operation times. Figure 8d shows η_V over the idle operation time measured at 20, 40, 60, and 80 mA cm⁻². As expected, η_V revealed very slight degradation. Only evident throughout the prolonged 400 h operation time, the efficiency at 80 mA cm⁻² decreased by 1.5%. Moreover, the deceleration from above implies that the degradation only shows in the first days and weeks of operation, suggesting that the battery will ultimately run at nearly constant performance in the long term.

In Fig. 8, the efficiency degradation was only resolvable under highly constant electrolyte conditions since R_{ct} was highly sensitive to temperature changes, as demonstrated in Figs. SI 6 and SI 7. Another supporting factor was the moderate electrolyte temperature of 20 °C. If measured at 30 °C instead of 20 °C, R_{ct} would have contributed 27% less to the overall cell resistance. Consequently, changes of R_{ct} would have been less evident, and the overall efficiency would have appeared even more stable over time. These observations may explain findings in the literature, reporting stable performance for activated GFD electrodes.²⁹ Conclusively, when assessing electrodes with sufficient TSA, the efficiency may indeed appear stable within given cell operation times.

In summary, although we were able to resolve the degradation of GF-HT, the drop in efficiency throughout 400 h was minor, being likely a result of the large TSA. Moreover, as the already low degradation decelerated, high and stable cell performance is in prospect for long-term operation.

Conclusions

We studied the effects of thermal treatment on VRF graphite felt electrodes after they were plasma-treated to ensure complete wettability. Compared to the sole plasma treatment, additional thermal treatment enhanced the electrode performance progressively, primarily due to surface corrosion increasing its roughness and total surface area (TSA). The corrosion presumably increased the number of carbon edge-plane surface sites catalyzing the V²⁺/V³⁺-reaction. The content of surface oxygen functionalities played no significant role.

Sole plasma treatment equipped the surface with the most oxygen functionalities. However, these electrodes showed the highest initial R_{ct} of 0.7 Ω cm², further suffering degradation by a 50% R_{ct} increase over 20 h idle cell operation. Additional to plasma, thermal treatment enhanced the performance significantly, evident in an R_{ct} eventually decreased by 78% after 24 h treatment. Simultaneously, the thermal

treatment decreased the surface content of oxygen functionalities from 16% to 8%, opposed to findings in the literature reporting the electrode performance to correlate with oxygen functionalities.

Instead, SEM imaging of the GF electrode surface indicated a roughening of the fiber surface. Krypton BET analysis revealed the TSA incrementally increased from $0.5 \text{ m}^2 \text{ g}^{-1}$ to $1.0 \text{ m}^2 \text{ g}^{-1}$. However, the TSA increase could still not explain the R_{ct} decrease in absolute measures. Therefore, we presume that the carbon surface corrosion causing the increased TSA and roughness had created carbon edge sites increasing the catalytic surface activity.

Addressing the performance degradation, we found that electrodes with a higher TSA showed a minor R_{ct} increase in absolute measures. However, in relative measures, the R_{ct} of each examined electrode increased similarly by 50% over the initial 20 h of operation, disregarding the TSA. Consequently, we examined the GF variant with the highest TSA of $6 \text{ m}^2 \text{ g}^{-1}$ for its long-term cell operation. Over 400 h, the R_{ct} increased by 300% from 0.1 to $0.3 \Omega \text{ cm}^2$, resulting in a cell voltage efficiency decrease from 92% to 90% at 80 mA cm^{-2} . The degradation rate decelerated significantly, indicating that the decreasing efficiency aims for eventually stable values. A recently proposed mechanism explaining the observed degradation due to V^{2+} surface adsorption supports this observation. Thereby, the formation of an equilibrium surface coverage by adsorbent suggests stable kinetics and constant long-term performance. Consequently, enlarging the TSA enhances the electrode performance at any time of cell operation.

In general, future studies on modifying electrode material should thoroughly investigate the changed surface properties. In particular, critical assessment should focus on whether the main improvement results from accumulated surface oxygen functionalities, improved wettability, increased TSA, or altered surface structure. Instead of surface oxygen enrichment, in our case, surface corrosion and concomitant TSA enlargement proved as the more effective strategy to exploit the full electrode performance potential. This strategy may lead the way to bring VRF batteries closer to their ultimate goal of finding their widespread use, contributing to an energy-rich but sustainable future.

Acknowledgments

This work was funded by the Bavarian Ministry of Economic Affairs and Media, Energy, and Technology through the project ZAE-ST (storage technologies). We thank Tobias Graf for his support with the electrochemical measurements and Hubert A. Gasteiger and Thomas J. Rabbow for valuable discussions.

ORCID

Tobias Greese  <https://orcid.org/0000-0002-7119-1647>

Paulette A. Loichet Torres  <https://orcid.org/0000-0001-7304-9110>

References

- D. Aaron, Z. Tang, A. B. Papandrew, and T. A. Zawodzinski, "Polarization curve analysis of all-vanadium redox flow batteries." *J. Appl. Electrochem.*, **41**, 1175 (2011).
- M. L. Perry and A. Z. Weber, "Advanced redox-flow batteries: a perspective." *J. Electrochem. Soc.*, **163**, A5064 (2015).
- M. Ulaganathan, V. Aravindan, Q. Yan, S. Madhavi, M. Skyllas-Kazacos, and T. M. Lim, "Recent advancements in all-vanadium redox flow batteries." *Adv. Mater. Interfaces*, **3**, 1500309 (2016).
- L. Yue, W. Li, F. Sun, L. Zhao, and L. Xing, "Highly hydroxylated carbon fibres as electrode materials of all-vanadium redox flow battery." *Carbon*, **48**, 3079 (2010).
- B. Sun and M. Skyllas-Kazacos, "Chemical modification of graphite electrode materials for vanadium redox flow battery application—part II. Acid treatments." *Electrochim. Acta*, **37**, 2459 (1992).
- H. Kabir, I. O. Gyan, and I. F. Cheng, "Electrochemical modification of a pyrolytic graphite sheet for improved negative electrode performance in the vanadium redox flow battery." *J. Power Sources*, **342**, 31 (2017).
- H. Liu, L. Yang, Q. Xu, and C. Yan, "An electrochemically activated graphite electrode with excellent kinetics for electrode processes of V (II)/V (III) and V (IV)/V (V) couples in a vanadium redox flow battery." *RSC Adv.*, **4**, 55666 (2014).
- W. Zhang, J. Xi, Z. Li, H. Zhou, L. Liu, Z. Wu, and X. Qiu, "Electrochemical activation of graphite felt electrode for $\text{VO}_2/\text{VO}_2 + \text{redox couple}$ application." *Electrochim. Acta*, **89**, 429 (2013).
- X. G. Li, K. L. Huang, S. Q. Liu, T. A. N. Ning, and L. Q. Chen, "Characteristics of graphite felt electrode electrochemically oxidized for vanadium redox battery application." *Transactions of Nonferrous Metals Society of China*, **17**, 195 (2007).
- D. Dixon, D. J. Babu, J. Langner, M. Bruns, L. Pfaffmann, A. Bhaskar, and H. Ehrenberg, "Effect of oxygen plasma treatment on the electrochemical performance of the rayon and polyacrylonitrile based carbon felt for the vanadium redox flow battery application." *J. Power Sources*, **332**, 240 (2016).
- L. Estevez, D. Reed, Z. Nie, A. M. Schwarz, M. I. Nandairi, J. P. Kizewski, and B. Li, "Tunable oxygen functional groups as electrocatalysts on graphite felt surfaces for all-vanadium flow batteries." *ChemSusChem*, **9**, 1455 (2016).
- K. J. Kim, Y. J. Kim, J. H. Kim, and M. S. Park, "The effects of surface modification on carbon felt electrodes for use in vanadium redox flow batteries." *Mater. Chem. Phys.*, **131**, 547 (2011).
- P. C. Ghimire, R. Schweiss, G. G. Scherer, T. M. Lim, N. Wai, A. Bhattarai, and Q. Yan, "Optimization of thermal oxidation of electrodes for the performance enhancement in all-vanadium redox flow batteries." *Carbon*, **155**, 176 (2019).
- A. M. Pezeshki, J. T. Clement, G. M. Veith, T. A. Zawodzinski, and M. M. Mench, "High performance electrodes in vanadium redox flow batteries through oxygen-enriched thermal activation." *J. Power Sources*, **294**, 333 (2015).
- B. Sun and M. Skyllas-Kazacos, "Modification of graphite electrode materials for vanadium redox flow battery application—I. Thermal treatment." *Electrochim. Acta*, **37**, 1253 (1992).
- Q. H. Liu, G. M. Grim, A. B. Papandrew, A. Turhan, T. A. Zawodzinski, and M. M. Mench, "High performance vanadium redox flow batteries with optimized electrode configuration and membrane selection." *J. Electrochem. Soc.*, **159**, A1246 (2012).
- P. Mazúr, J. Mrlík, J. Beneš, J. Pociđič, J. Vrána, J. Dundálek, and J. Kosek, "Performance evaluation of thermally treated graphite felt electrodes for vanadium redox flow battery and their four-point single cell characterization." *J. Power Sources*, **380**, 105 (2018).
- R. Schweiss, C. Meiser, and F. W. T. Goh, "Steady-state measurements of vanadium redox-flow batteries to study particular influences of carbon felt properties." *ChemElectroChem*, **4**, 1969 (2017).
- M. A. Miller, A. Bourke, N. Quill, J. S. Wainright, R. P. Lynch, D. N. Buckley, and R. F. Savinell, "Kinetic study of electrochemical treatment of carbon fiber microelectrodes leading to in situ enhancement of vanadium flow battery efficiency." *J. Electrochem. Soc.*, **163**, A2095 (2016).
- Y. Li, J. Parrondo, S. Sankarasubramanian, and V. Ramani, "Impact of surface carbonyl-and hydroxyl-group concentrations on electrode kinetics in an all-vanadium redox flow battery." *The Journal of Physical Chemistry C*, **123**, 6370 (2019).
- N. Bevilacqua, L. Eifert, R. Banerjee, K. Köble, T. Faragó, M. Zuber, and R. Zeis, "Visualization of electrolyte flow in vanadium redox flow batteries using synchrotron X-ray radiography and tomography—Impact of electrolyte species and electrode compression." *J. Power Sources*, **439**, 227071 (2019).
- T. J. Rabbow, M. Trampert, P. Pokorny, P. Binder, and A. H. Whitehead, "Variability within a single type of polyacrylonitrile-based graphite felt after thermal treatment. Part I: physical properties." *Electrochimica Acta*, **173**, 17 (2015).
- T. J. Rabbow, M. Trampert, P. Pokorny, P. Binder, and A. H. Whitehead, "Variability within a single type of polyacrylonitrile-based graphite felt after thermal treatment. Part II: chemical properties." *Electrochim. Acta*, **173**, 24 (2015).
- X. Chu and K. Kinoshita, "Surface modification of carbons for enhanced electrochemical activity." *Materials Science and Engineering: B*, **49**, 53 (1997).
- P. Mazúr, J. Mrlík, J. Pociđič, J. Vrána, J. Dundálek, J. Kosek, and T. Bystron, "Effect of graphite felt properties on the long-term durability of negative electrode in vanadium redox flow battery." *J. Power Sources*, **414**, 354 (2019).
- I. Derr, A. Fetyan, K. Schütjajew, and C. Roth, "Electrochemical analysis of the performance loss in all vanadium redox flow batteries using different cut-off voltages." *Electrochim. Acta*, **224**, 9 (2017).
- I. Derr, D. Przyrembel, J. Schweer, A. Fetyan, J. Langner, J. Melke, and C. Roth, "Electroless chemical aging of carbon felt electrodes for the all-vanadium redox flow battery (VRFB) investigated by electrochemical impedance and X-ray photoelectron spectroscopy." *Electrochim. Acta*, **246**, 783 (2017).
- A. M. Pezeshki, R. L. Sacci, G. M. Veith, T. A. Zawodzinski, and M. M. Mench, "The cell-in-series method: A technique for accelerated electrode degradation in redox flow batteries." *J. Electrochem. Soc.*, **163**, A5202 (2015).
- O. Nibel, S. M. Taylor, A. Pátru, E. Fabbri, L. Gubler, and T. J. Schmidt, "Performance of different carbon electrode materials: insights into stability and degradation under real vanadium redox flow battery operating conditions." *J. Electrochem. Soc.*, **164**, A1608 (2017).
- T. Greese and G. Reichenauer, "Anode kinetics degradation in vanadium redox flow batteries—Reversible inhibition of the V_2/V_3+ -reaction due to V (II)-adsorption." *J. Power Sources*, **500**, 229958 (2021).
- P. Mazúr, J. Mrlík, J. Beneš, J. Pociđič, J. Vrána, J. Dundálek, and J. Kosek, "Performance evaluation of thermally treated graphite felt electrodes for vanadium redox flow battery and their four-point single cell characterization." *J. Power Sources*, **380**, 105 (2018).
- H. Fink, *Untersuchung von Verlustmechanismen in Vanadium-Flussbatterien*, Technische Universität München (2019), Doctoral dissertation <https://mediatum.ub.tum.de/doc/1471866/1471866.pdf>.
- J. Langner, J. Melke, H. Ehrenberg, and C. Roth, "Determination of overpotentials in all vanadium redox flow batteries." *ECS Trans.*, **58**, 1 (2014).
- C. N. Sun, F. M. Delnick, D. S. Aaron, A. B. Papandrew, M. M. Mench, and T. A. Zawodzinski Jr, "Resolving losses at the negative electrode in all-vanadium

- redox flow batteries using electrochemical impedance spectroscopy." *J. Electrochem. Soc.*, **161**, A981 (2014).
35. J. Landesfeind, D. Pritzl, and H. A. Gasteiger, "An analysis protocol for three-electrode li-ion battery impedance spectra: Part I. analysis of a high-voltage positive electrode." *J. Electrochem. Soc.*, **164**, A1773 (2017).
 36. J. H. Scofield, "Hartree-Slater subshell photoionization cross-sections at 1254 and 1487 eV." *J. Electron. Spectrosc. Relat. Phenom.*, **8**, 129 (1976).
 37. A. Jablonski and C. J. Powell, *NIST Electron Effective-Absorption-Length Database*, National Institute of Standards and Technology (2011), Doctoral Dissertation <https://www.nist.gov/system/files/documents/srd/SRD82UsersGuideV1-3.pdf>.
 38. L. Eifert, R. Banerjee, Z. Jusys, and R. Zeis, "Characterization of carbon felt electrodes for vanadium redox flow batteries: Impact of treatment methods." *J. Electrochem. Soc.*, **165**, A2577 (2018).
 39. J. L. Figueiredo, M. F. R. Pereira, M. M. A. Freitas, and J. J. M. Orfao, "Modification of the surface chemistry of activated carbons." *Carbon*, **37**, 1379 (1999).
 40. B. Sun and M. Skyllas-Kazacos, "Modification of graphite electrode materials for vanadium redox flow battery application—I. Thermal treatment." *Electrochim. Acta*, **37**, 1253 (1992).
 41. O. Di Blasi, N. Briguglio, C. Busacca, M. Ferraro, V. Antonucci, and A. Di Blasi, "Electrochemical investigation of thermally treated graphene oxides as electrode materials for vanadium redox flow battery." *Appl. Energy*, **147**, 74 (2015).
 42. P. Chen, M. A. Fryling, and R. L. McCreery, "Electron transfer kinetics at modified carbon electrode surfaces: the role of specific surface sites." *Anal. Chem.*, **67**, 3115 (1995).
 43. D. J. Johnson, "Structure and properties of carbon fibres." In *Carbon Fibers Filaments and Composites*. (Springer, Berlin: Dordrecht) 119 (1990).
 44. S. Maass, F. Finsterwalder, G. Frank, R. Hartmann, and C. Merten, "Carbon support oxidation in PEM fuel cell cathodes." *J. Power Sources*, **176**, 444 (2008).
 45. J. Langner, M. Bruns, D. Dixon, A. Nefedov, C. Wöll, F. Scheiba, and J. Melke, "Surface properties and graphitization of polyacrylonitrile based fiber electrodes affecting the negative half-cell reaction in vanadium redox flow batteries." *J. Power Sources*, **321**, 210 (2016).
 46. C. E. Banks, T. J. Davies, G. G. Wildgoose, and R. G. Compton, "Electrocatalysis at graphite and carbon nanotube modified electrodes: edge-plane sites and tube ends are the reactive sites." *Chem. Commun.*, **7**, 829 (2005).
 47. W. Yuan, Y. Zhou, Y. Li, C. Li, H. Peng, J. Zhang, and G. Shi, "The edge-and basal-plane-specific electrochemistry of a single-layer graphene sheet." *Sci. Rep.*, **3**, 1 (2013).
 48. G. Wei, M. Jing, X. Fan, J. Liu, and C. Yan, "A new electrocatalyst and its application method for vanadium redox flow battery." *J. Power Sources*, **287**, 81 (2015).
 49. N. Pour, D. G. Kwabi, T. Carney, R. M. Darling, M. L. Perry, and Y. Shao-Horn, "Influence of edge-and basal-plane sites on the vanadium redox kinetics for flow batteries." *The Journal of Physical Chemistry C*, **119**, 5311 (2015).
 50. T. J. Rabbow and A. H. Whitehead, "Deconvolution of electrochemical double layer capacitance between fractions of active and total surface area of graphite felts." *Carbon*, **111**, 782 (2017).
 51. J.-P. Randin and E. Yeager, "Differential capacitance study of stress-annealed pyrolytic graphite electrodes." *J. Electrochem. Soc.*, **118**, 711 (1971).
 52. J. P. Randin and E. Yeager, "Differential capacitance study on the basal plane of stress-annealed pyrolytic graphite." *J. Electroanal. Chem. Interfacial Electrochem.*, **36**, 257 (1972).
 53. J. P. Randin and E. Yeager, "Differential capacitance study on the edge orientation of pyrolytic graphite and glassy carbon electrodes." *J. Electroanal. Chem. Interfacial Electrochem.*, **58**, 313 (1975).
 54. D. M. Kabtamu, J. Y. Chen, Y. C. Chang, and C. H. Wang, "Water-activated graphite felt as a high-performance electrode for vanadium redox flow batteries." *J. Power Sources*, **341**, 270 (2017).
 55. I. Derr, M. Bruns, J. Langner, A. Fetyan, J. Melke, and C. Roth, "Degradation of all-vanadium redox flow batteries (VRFB) investigated by electrochemical impedance and X-ray photoelectron spectroscopy: Part 2 electrochemical degradation." *J. Power Sources*, **325**, 351 (2016).